Bio-inorganic hybrid photoanodes of Photosystem II and ferricyanide-intercalated layered double hydroxide for visible-light-driven water oxidation

Masaru Kato,*[a,b] Hisako Sato,[c] Ichizo Yagi,[a] Miwa Sugiura*[b,d]

[a] Section of Environmental Materials Science, Faculty of Environmental Earth Science, Hokkaido University, N10W5, Kita-ku, Sapporo 060-0810, Japan.

[b] Proteo-Science Center, Ehime University, 3 Bunkyo-cho, Matsuyama, Ehime 790-8577 Japan.

[c] Department of Chemistry, Graduate School of Science and Engineering, Ehime University, 2-5 Bunkyo-cho, Matsuyama, Ehime 790-8577, Japan.

[d] PRESTO, Japan Science Technology Agency (JST), 4-1-8, Honcho, Kawaguchi, Saitama 332-0012, Japan.

*Corresponding author. Tel.: +81 11 706 2276.

E-mail address: masaru.kato@ees.hokudai.ac.jp (M.K.); miwa.sugiura@ehime-u.ac.jp (M.S.)

Abstract

Photosynthesis converts solar energy into chemical energy. Photosystem II (PSII) oxidizes water to produce oxygen, electrons and protons under solar light irradiation. This light-driven water oxidation initiates a series of reactions in photosynthesis. Basic photoelectrochemical studies on PSII are directed toward the enzymatic applications of PSII for sustainable production of electricity or solar fuels. To maximize the photoelectrochemical catalytic activity of PSII on electrode substrates, interfacial designs between PSII and electrode substrates are important. Herein, we report bio-inorganic photoanodes of PSII and ferricyanide-intercalated layered double hydroxide (LDH) for visible-light-driven water oxidation. PSII is simply drop-cast onto a ferricyanide-intercalated Cobalt–Aluminum LDH and then shows a turnover frequency of 0.5±0.1 s^{-1} and a turnover number of 920 ± 40 for 1 h at pH 6.5 at +0.5 V vs. NHE under visible light irradiation. Photoelectrochemical experiments using a PSII inhibitor or a bio-engineered PSII suggest that interfacial electron transfer from the plastoquinone Q_A site of PSII to ferricyanide may play an important role in improving the photo-electrocatalytic activity and stability of PSII. Our studies will open up new possibilities in fundamental or advanced photoelectrochemical studies of PSII.

Keywords

Photosystem II; Layered double hydroxide; Oxygen evolution reaction; Artificial photosynthesis; Photoanode

1. Introduction

Photosystem II (PSII) is a photosynthetic enzyme and found in oxygenic photosynthetic organisms such as plants, algae and cyanobacteria. This enzyme is able to absorb solar light and then to split water molecules into oxygen molecules, protons and electrons. Since PSII is the only known water oxidation enzyme, understanding its protein structure [1, 2] and reaction mechanism [3] inspires us to develop PSII-based photochemical devices [4-6] or PSII-inspired artificial water oxidation catalysts [7-12] for the sustainable production of solar fuels.

To study PSII on its efficient photocatalytic water oxidation or complicated internal electron transfer relay [13], PSII is isolated from oxygenic photosynthetic organisms such as thermophilic cyanobacteria. The isolated PSII, however, is quite unstable under light irradiation because it has neither repairing machinery nor electron acceptors for photo-excited electrons, which cause the degradation of PSII [14, 15]. Thus, the isolated PSII must be carefully handled in the dark until photochemical experiments, and exogenous electron acceptors such as 1,4-quinone derivatives [16, 17], transition metal complexes [6, 17-19] and redox proteins [20, 21] are necessary during photochemical experiments, where electron acceptors extract electrons from PSII and maintain photocatalytic cycles of PSII.

For photoelectrochemical studies on PSII, electrode substrates work as electron acceptors and extract photo-excited electrons generated in PSII on electrode substrates, resulting in photocurrent generation involving oxygen evolution catalyzed by PSII. The slow electron transfer kinetics from PSII to the electrode substrate is known to cause photo-degradation of PSII. Thus, electrode substrates used are important to achieve high photocatalytic activity and stability of PSII photoanodes. Many electrode materials such as indium-tin oxide [5, 22-24], titanium dioxide [25, 26], Ti-doped Fe_2O_3 [27] and redox polymer [4, 24, 28-30] have been studied on PSII photoanodes. Two interfacial electron transfer pathways to the electrode substrate are known from the primary plastoquinone Q_A and from the secondary plastoquinone Q_B [22]. The internal electron transfer from Q_A to Q_B in PSII is a slow electron transfer process and is known to cause photodamage to PSII [13, 31]. Thus, the use of electrode substrates that are able to efficiently pick up photo-excited electrons from the Q_A site of PSII might improve photo-activity and stability of PSII photoanodes, possibly opening up new possibilities in enzymatic photovoltaic or water splitting devices with PSII [4, 5].

Herein, we report photocatalytic activity and stability of bio-inorganic photoanodes of PSII for visible-light-driven water oxidation (Fig. 1). PSIIs were isolated from *Thermosynecococcus elongatus (T. elongatus)*, and immobilized on

ferricyanide ($[Fe^{III}(CN)_6]^{3-}$)-intercalated layered double hydroxides (LDHs) on indium–tin oxide (ITO) substrates. Ferricyanide is negatively charged and works as an electron acceptor from the Q_A site [17]. LDHs consist of cationic double hydroxide nanosheets and exchangeable anions and have been studied for applications such as electrode materials or catalysts [32-36]. In this work, we have prepared LDH-modified ITO substrates, intercalated ferricyanide into the LDH cationic nanosheets and then simply drop-cast PSII on the ferricyanide-intercalated LDH substrates to record photocurrent responses of them under visible light irradiation.

2. Experimental

2.1. Materials

Solvents and metal nitrates including $Al(NO_3)_3 \cdot 9H_2O$, $Mg(NO_3)_2 \cdot 6H_2O$ and $Co(NO_3)_2 \cdot 6H_2O$ were purchased from Nacalai Tesque, Inc. or Wako Pure Chemical Industries, Ltd., and used without further purification. Potassium ferricyanide ($K_3[Fe(CN)_6]$), 3-(3,4-dichlorophenyl)-1,1-dimethylurea (DCMU) and 2,6-dichloro-1,4-benzoquinone (DCBQ) were purchased from Aldrich. ITO-coated glass slides (IN-100, 10 Ω cm^{-2}) were purchased from Furuuchi Chemical Corporation. Mn-depleted PSII was prepared using tris(hydroxymethyl)aminomethane according to

the literature [37].

2.2. Isolation of PSII complexes from *T. elongatus* mutants

PSII core complexes were isolated from the *T. elongatus* strain cells by a Ni^{2+}-affinity chromatography after solubilization of thylakoid membranes with *n*-dodecyl *β*-D-maltoside as described in the literature [17]. Two types of PSII were isolated from *T. elongatus* mutants. One type of PSII has PsbA1 as the D1 protein encoded by the $psbA_1$ gene [38] and used for our standard photoelectrochemical experiments. Another type of PSII has PsbA3 as the D1 protein encoded by the $psbA_3$ gene ($PSII_{PsbA3}$) [16]. Both types have a His_6-tag on the C-terminus of the CP43 protein of the PSII complex.

O_2 evolution activities of isolated PSII and $PSII_{PsbA3}$ in solution were determined using a Clark-type electrode (CB1-D, HANSATECH). Oxygen evolution of PSII (4 μg Chl mL^{-1}) was measured in a buffered solution containing 40 mM 2-(*N*-morpholino)ethanesulfonic acid (MES), 15 mM $CaCl_2$, 15 mM $MgCl_2$ and 100 mM NaCl at pH 6.5 at 25 °C under saturating white light. A projector (PROCABIN 67-Z, CABIN) equipped with water and IR filters was used as a light source. $K_3[Fe^{III}(CN)_6]$ (the final concentration: 2 mM) or 2,6-dichloro-1,4-benzoquinone (DCBQ) (dissolved in dimethyl sulfoxide; the final concentration: 1 mM) was used as

an electron acceptor in the buffered solution. PSII and $PSII_{PsbA3}$ produced oxygen under light irradiation at $(3.8\pm0.2)\times10^3$ μmol O_2 mg Chl^{-1} h^{-1} and $(2.6\pm0.2)\times10^3$ μmol O_2 mg Chl^{-1} h^{-1}, respectively, in the presence of 1 mM DCBQ, while PSII and $PSII_{PsbA3}$ evolved oxygen at $(0.84\pm0.06)\times10^3$ μmol O_2 mg Chl^{-1} h^{-1} and $(0.31\pm0.04)\times10^3$ μmol O_2 mg Chl^{-1} h^{-1}, respectively, in the presence of 2 mM $K_3[Fe^{III}(CN)_6]$.

2.3. Preparation of MgAl–CO_3 LDH on ITO

MgAl–CO_3 LDHs was directly grown on ITO-coated glass slides using a slightly modified method described in the literature [39]. $Mg(NO_3)_2\cdot6H_2O$ (0.86 g, 3.3 mmol), $Al(NO_3)_3\cdot9H_2O$ (0.62 g, 1.7 mmol) and urea (2.8 g, 47 mmol) were dissolved in 10 mL of water and the mixture was stirred for at least 30 min. ITO-coated glass slides (1×2 cm^2) were sequentially sonicated in soapy water, water, acetone, ethanol and water for 10 min each and dried under air before use. The solution was transferred to a Teflon-lined autoclave, and the clean ITO slides were vertically placed in the solution. The autoclave was sealed and heated in an oven at 90 °C for 9 h. After that, the autoclave was naturally cooled to room temperature in the oven. The resulting MgAl–CO_3 LDH/ITO slides were taken out from the autoclave, rinsed with water and then dried under air.

2.4. Preparation of CoAl–CO_3 LDH on ITO

CoAl–CO_3 LDHs were directly grown on ITO-coated glass slides according to the literature [33]. ITO-coated glass slides (1×2 cm^2) were sequentially cleaned by sonicating with soapy water, water, acetone, ethanol and water for 10 min each before use. $Co(NO_3)_2 \cdot 6H_2O$ (0.29 g, 1.0 mmol), $Al(NO_3)_3 \cdot 9H_2O$ (0.19 g, 0.5 mmol), NH_4F (0.18 g, 5.0 mmol) and urea (2.10 g, 35 mmol) were dissolved in 50 mL of water and the solution was stirred for at least 30 min at room temperature. The mixture (20 mL) was transferred to a Teflon-lined autoclave and the cleaned ITO slides were vertically placed in the solution. The autoclave was sealed and heated at 95°C for 6 h. After that, the autoclave was naturally cooled to room temperature in the oven. The resulting CoAl–CO_3 LDH/ITO slides were removed from the autoclave, rinsed with water and dried at room temperature under air.

2.5. Decarbonization and anion exchange for MAl–CO_3 LDH to obtain MAl–$[Fe(CN)_6]$ (M = Mg or Co)

The decarbonization of the as-prepared MAl–CO_3 LDH/ITO was carried out by treating with a salt-acid mixed solution as described in the literature [40, 41]. One slide of MAl–CO_3 LDH/ITO was immersed in a degassed aqueous solution containing 1 M NaCl and 0.43 mM HCl (2.3 mL), and then the slide was kept under nitrogen at room temperature for 3 h. The resulting slide (MAl–Cl LDH, M = Mg or Co) was rinsed with

water and ethanol and then dried under air.

Next, two slides of MAl–Cl LDH/ITO were placed in 2 mL of a degassed aqueous $K_3[Fe^{III}(CN)_6]$ solution (0.1 M) and kept at room temperature under nitrogen for 3 h and 12 h to obtain CoAl–$[Fe(CN)_6]$ LDH and MgAl–$[Fe(CN)_6]$ LDH, respectively. The resulting slides were rinsed with water and ethanol and then dried under air.

2.6. Characterization of MAl–$[Fe(CN)_6]$ LDH on ITO (M = Mg or Co)

MAl–X LDHs (M = Mg or Co; X = CO_3 or $[Fe(CN)_6]$) on ITO slides were characterized by using X-ray diffraction (XRD), infrared (IR) spectroscopy, field emission scanning electron microscopy (SEM) and energy-dispersive X-ray spectroscopy (EDS).

XRD patterns of MAl–X LDHs on ITO slides were recorded with a Rigaku Ultima IV diffractometer equipped with graphite monochromatized Cu Kα radiation (λ = 0.1541841 nm). All data were collected at 40 kV, 40 mA, a scanning rate of 3° min^{-1} and a step size of 0.01° in the 2θ angle range from 2° to 70°. A JEOL FE-SEM JSM-7001F equipped with an energy dispersive X-ray spectrometer was used for morphology observation and EDS analysis of the MAl–X LDHs on ITO slides. IR spectra of MAl–X LDHs scraped from ITO were recorded on a Thermo Scientific

Nicolet iS5 FT-IR spectrometer using an iD5 Diamond ATR accessory.

2.7. Electrochemical measurements

All electrochemical measurements were carried out using an Ivium CompactStat potentiostat. A conventional three-electrode setup was used: the platinum mesh counter electrode, the Ag|AgCl (3 M NaCl) reference electrode and a working electrode. Buffered aqueous solution containing 40 mM MES, 15 mM $CaCl_2$, 15 mM $MgCl_2$ and 100 mM NaCl (pH 6.5) was used as the electrolyte solution for standard photocurrent measurements. The electrolyte solution at pH 6.5 was used because the catalytic activity of PSII is known to maximize at pH 6.5 [42]. For experiments on diffusional $[Fe^{III}(CN)_6]^{3-}$, an aqueous electrolyte solution containing 40 mM MES, 15 mM $CaCl_2$, 15 mM $MgCl_2$, 100 mM NaCl and 2 mM $K_3[Fe^{III}(CN)_6]$ at pH 6.5 was used. All electrochemical data were recorded at 24 °C. A light source of MME-250 (SCHOTT MORITEX Corporation) was used with an IR and a red-pass filter (> 600 nm) for standard photoelectrochemical measurements. Light intensities were determined using a light meter (LI-250A, LI-COR Biosciences). All potentials vs Ag|AgCl (3 M NaCl) were converted to NHE by adding +0.21 V. The geometrical surface area exposed to the electrolyte solution was 0.5 cm^2. All photocurrent densities reported in this work are normalized to the projected geometrical surface area of the electrode.

For photocurrent action spectrum measurements, a xenon light source MAX-303 (300 W, Asahi Spectra Co., Ltd.) equipped with a mirror module for visible light irradiation (450 nm−800 nm) was used as a light source. Band pass filters (MX0600−MX0720, Asahi Spectra Co., Ltd.) were also used to obtain visible light with a specific wavelength. Light intensities were measured and adjusted using a power meter PM30 (THORLABS, Inc.) with a power sensor S120UV (THORLABS, Inc.).

2.8. Immobilization of PSII on electrodes

After control experiments of an LDH electrode without PSII, the electrode was taken out from the electrochemical cell and 1 μL of a PSII solution (3.7 mg Chl mL^{-1} for the standard PSII and 3.9 mg Chl mL^{-1} for $PSII_{PsbA3}$) was drop-cast on the electrode. The electrode was kept at room temperature in the dark for 10 min and rinsed with 1 mL of the electrolyte solution.

2.9. Determination of photocurrent densities, incident-photon-to-current conversion efficiency, turnover frequencies and turnover numbers of PSII–LDH electrodes

Photocurrent responses of PSII–LDH electrodes were recorded with three or four light cycles of light irradiation for 3 min followed by the dark for 3 min each. Photocurrent intensities are defined as the difference between the dark current before

the start of irradiation and the photocurrent before the end of irradiation (i.e., 3 min after the start of irradiation).

Incident-photon-to-current conversion efficiencies (IPCEs) were determined using the following equation [26]: $\eta(\%) = \{1240 \times j\ (\mu A\ cm^{-2})\} / \{P\ (W\ m^{-2}) \times \lambda\ (nm)\}$, where j, P and λ denote a photocurrent density, the incident photon flux and the wavelength of the incident light, respectively. All incident photons were assumed to be absorbed by the photoanode.

Turnover frequencies (TOFs) were calculated based on photocurrent densities and amounts of PSII immobilized on the electrode. PSII immobilized on the electrode was quantified based on amounts of chlorophyll *a* (Chl *a*) extracted from PSII. To extract Chl *a* from PSII immobilized on PSII photoanodes after photoelectrochemical measurements, LDHs were dispersed in 350 μL of a MeOH–H_2O mixture (8:2, *v*/*v*) and centrifuged at 7300×*g* for 5 min (TOMY high micro centrifuge MC-150, TOMY TMA-2 rotor). UV-vis absorption spectra of the supernatant were recorded on a Hitachi U 2810 UV-vis spectrometer. The number of PSII immobilized on each electrode was quantified from the absorbance at 665 nm (ε = 79.95 (mg Chl *a*)$^{-1}$ mL cm^{-1}) [43] and the number of Chl *a* in PSII (35 Chl *a* per PSII monomer) [2].

Turnover numbers (TONs) were determined based on the amount of PSII

immobilized and the number of electrons that passed between the working electrode and the counter electrode, assuming that all PSIIs immobilized were active and all electrons were used for the oxygen evolution catalyzed by PSII (four electrons for one oxygen molecule).

For Photocurrent measurements in the presence of DCMU, dimethyl sulfoxide solution containing 0.1 M DCMU (50 μL) was added to the electrolyte solution (5 mL). The final concentration of DCMU was 1 mM.

2.10. Data analysis

All experiments were carried out at least three times with different samples. The data were analysed as follows: considering a sample of n observations x_i, the unweighted mean value (x_u) along with its standard deviation (σ) was calculated using the following equations: $x_u = \Sigma_i x_i/n$; $\sigma = \{\Sigma_i(x_i-x_u)^2/[n(n-1)]\}^{1/2}$.

3. Results and discussion

LDHs were directly grown on ITO-coated glass substrates based on a urea hydrolysis method, which provides strong adhesion between LDH and the substrate and is suitable for preparation of LDH-modified electrodes [32, 33, 39]. Two types of LDH, magnesium–aluminum and cobalt–aluminium LDHs (MAl–X LDHs: M = Mg or Co, X = intercalated anions such as CO_3^- and $[Fe^{III}(CN)_6]^-$), were selected in this work to

understand effects of electroactive Co^{II} ions and non-electroactive Mg^{II} in LDHs on the electron transfer [44]. Scanning electron microscopy (SEM) images revealed that as-prepared LDHs were vertically grown on ITO with film thicknesses of ca. 0.6 μm for MgAl–CO_3 LDH and ca. 3.3 μm for CoAl–CO_3 LDH (Fig. 2). IR spectra of the MgAl–CO_3 and CoAl–CO_3 LDHs exhibited peaks at 1349 cm^{-1} and 1363 cm^{-1}, respectively (Fig. S1, see Supplementary Data). These peaks are assigned to the vibration mode of the intercalated CO_3^{2-}, which originate from the dissolved carbon dioxide released during the urea hydrolysis. XRD patterns of the as-prepared LDHs showed characteristic peaks at $2\theta \approx 12°$ for the (003) diffraction, corresponding to a basal distance of 0.76 nm (Fig. S2), indicating the intercalation of carbonate anions into LDHs [41]. Energy dispersive X-ray spectroscopy measurements confirmed the molar ratios of M to Al: approximately 1:1 for the MgAl–CO_3 LDH and 3:1 for the CoAl–CO_3 LDH.

Next, carbonate anions in the as-prepared MAl–CO_3 LDHs were exchanged with ferricyanide to obtain ferricyanide-intercalated LDHs on ITO (MAl–[$Fe(CN)_6$], M = Mg or Co). The anion-exchange was carried out in two steps: the replacement of carbonate by chloride using a NaCl–HCl mixed solution [40, 41], followed by ferricyanide using 0.1 M $K_3[Fe^{III}(CN)_6]$ aqueous solution [45] because carbonate anions are tightly bound

to the interlayers of LDHs [40]. IR spectra of MAl–[$Fe(CN)_6$] LDHs showed peaks at around 2038 cm^{-1} (Fig. S1), corresponding to the stretching vibration of $[Fe^{II}(CN)_6]^{4-}$ species [45]. Peak shifts for the (003) diffraction to lower 2θ angles were observed in XRD patterns after the anion exchange (Fig. S2), indicating that the increase in basal distance involved the intercalation of ferricyanide, which is larger than carbonate [45]. The XRD pattern of CoAl–[$Fe(CN)_6$] also showed peak broadening, compared with that of the as-prepared one, suggesting that the crystallinity decreased during the intercalation process, although no obvious morphology change was observed in SEM images (Fig. S3). Cyclic voltammograms of MAl–[$Fe(CN)_6$] showed redox waves (Fig. S4) while MAl–CO_3 in the absence of the intercalated ferricyanide show no redox wave (Fig. S5a), clearly indicating that the redox waves observed for MAl–[$Fe(CN)_6$] originated from ferricyanide anions that were intercalated into LDHs. The peak positions of the redox waves observed for MAl–[$Fe(CN)_6$ were different from those of the redox couple of ferricyanide in the electrolyte solution (Fig. S5b), which means that the electron transfer rate of ferricyanide might be influenced by the interaction, compared with that in solution.

Photocurrent responses of PSII-modified and unmodified electrodes were recorded at +0.5 V vs NHE at pH 6.5 under red light irradiation (Fig. 3A). The

photocurrent measurements have revealed that the intact PSII is required to observe photocurrent responses. The MAl–$[Fe(CN)_6]$ LDH electrodes without PSII showed no photocurrent (Fig. 3A). CoAl–$[Fe(CN)_6]$ modified with Mn-depleted PSII, which lacks the oxygen evolving complex of the Mn_4CaO_5 cluster [37], gave rise to almost no photocurrent (Fig. 3A). A photocurrent action spectrum of CoAl–$[Fe(CN)_6]$|PSII was recorded and in good agreement with the absorption spectrum of PSII (Fig. 4). These results allow us to confirm that photocurrent responses originate from photoelectrochemical water oxidation driven by PSII. An incident-photon-to-current conversion efficiency (IPCE) at 680 nm was determined to be approximately 0.010% for CoAl–$[Fe(CN)_6]$|PSII.

Control experiments confirm that the use of not only the intact PSII but also ferricyanide is important to observe photocurrent responses in our system. MAl–CO_3 electrodes modified with PSII showed almost no photocurrent, whereas MAl–$[Fe(CN)_6]$ with PSII did (Fig. 3A). Since MAl LDHs are insulators, it is most likely that the intercalated ferricyanide anions mediate the electron transfer from the PSII to the ITO substrate. A minimum bias potential of +0.4 V vs. NHE was required to observe photocurrent responses (Fig. S6).

Table 1 summarizes photocurrent densities, amounts of PSII immobilized on the

electrodes and turnover frequencies (TOFs) of PSII on MAl–$[Fe(CN)_6]$. More PSII was immobilized on CoAl–$[Fe(CN)_6]$ rather than on MgAl–$[Fe(CN)_6]$. This is in good agreement with the thickness of MAl LDH on ITO (Fig. 2). Photocurrent densities and amounts of PSII allowed us to calculate TOFs of PSII (Table 1). The TOF of PSII on CoAl–$[Fe(CN)_6]$ ($0.5\pm0.1\ s^{-1}$) was higher than that on MgAl–$[Fe(CN)_6]$ ($0.07\pm0.03\ s^{-1}$). The redox active cobalt ions in the cationic CoAl nanosheets might improve the charge transport in LDHs [44]. This is why the TOF of PSII on CoAl–$[Fe(CN)_6]$ may be higher than that on MgAl–$[Fe(CN)_6]$. Interestingly, the TOF of PSII on CoAl–$[Fe(CN)_6]$ is comparable with that previously reported for PSII immobilized on a mesoporous ITO electrode ($0.6\pm0.1\ s^{-1}$), where the orientation of PSII was controlled and covalently bonded on the electrode surface [23]. In our system, PSII was simply drop-cast on CoAl–$[Fe(CN)_6]$ and showed such a comparable TOF. This result might be related to efficient interfacial electron transfer from PSII to CoAl–$[Fe(CN)_6]$ and/or orientation of PSII on the cationic LDH nanosheets. In a previous report, the co-immobilization of PSII with a redox-active osmium polymer gave a TOF of up to $4.0\pm0.1\ s^{-1}$ [24], which is higher than the TOF reported in this work. These results suggest that some PSII complexes on CoAl–$[Fe(CN)_6]$ have orientations that are unfavorable for the interfacial electron transfer.

To gain insights into the interfacial electron transfer, an herbicide DCMU was added into the electrolyte solution and then photocurrent responses of CoAl–$[Fe(CN)_6]$|PSII were recorded. DCMU is known to serve as an electron transfer inhibitor from Q_A to Q_B [21, 46]. Even in the presence of DCMU, photocurrent densities of 1.3±0.02 μA cm^{-2}, corresponding to approximately 56% of the residual photocurrent response, were observed (Table 1). This percentage is higher than that previously reported on a PSII–ITO photoanode (~30%) [22]. Thus, the CoAl–$[Fe(CN)_6]$|PSII photoanode may have the Q_A interfacial electron transfer pathway as the main pathway.

For a further understanding of the interfacial electron transfer, we used another type of PSII, termed $PSII_{PsbA3}$ and recorded photocurrent responses of CoAl–$[Fe(CN)_6]$|$PSII_{PsbA3}$. $PSII_{PsbA3}$ has the D1 protein subunit encoded by the *psbA*$_3$ gene [16, 38, 47] and the difference of 21 amino acids in the D1 protein subunit (Fig. S7 and Table S1) causes the positive redox potential shift of Q_A in $PSII_{PsbA3}$ (–102 ± 2 mV vs NHE [48]). In other words, $PSII_{PsbA3}$ has less driving force for the Q_A interfacial electron transfer than the standard PSII. CoAl–$[Fe(CN)_6]$|$PSII_{PsbA3}$ gave rise to a photocurrent density of 1.0±0.3 μA cm^{-2}, corresponding to a TOF of 0.18±0.04 (mol O_2) (mol PSII)$^{-1}$ s^{-1}, which was lower than that of the standard PSII (Table 1). This

result may come from the difference in driving force for the interfacial electron transfer from Q_A.

Finally, the photocurrent stability of CoAl–$[Fe(CN)_6]$|PSII was studied at +0.5 V vs NHE under continuous red light irradiation for 1 h (Fig. 3B) to demonstrate an advantage of the improvement of the Q_A interfacial electron transfer. The photoanode showed a relative photocurrent of > 50% after light irradiation of 1 h ($t_{1/2}$ > 1 h), which was much greater photocurrent stability than a PSII–ITO photoanode previously reported ($t_{1/2}$~12 min) [22]. Thanks to the improved photocurrent stability, a turnover number (TON) of PSII was determined to be 920 ± 40 mol O_2 (mol PSII)$^{-1}$ for 1 h under continuous visible light irradiation.

Although the value of TON determined in this work is close to that reported for PSII co-immobilized with the osmium polymer (946±96 mol O_2 (mol PSII)$^{-1}$) [24], much lower than that of TON = 3751 previously reported for a water splitting nanocolloidal system consisting of PSII, Ru/$SrTiO_3$:Rh and a redox shuttle of $[Fe(CN)_6]^{3-/4-}$ [6], where diffusional redox mediators of $[Fe(CN)_6]^{3-/4-}$ in solution are able to extract photo-electrons from almost all PSII. In our system, the redox mediator of $[Fe(CN)_6]^{3-/4-}$ is fixed and PSII may have random orientations at the electrode interface as mentioned above. Thus, only PSII with orientations suitable for the

interfacial electron transfer may function for photocurrent production on the electrode [23]. To neglect the PSII orientation effect on the photoelectrochemical activity of PSII photoanodes, we also carried out photocurrent stability measurements of CoAl–CO_3|PSII using the electrolyte solution containing 2 mM $K_3[Fe^{III}(CN)_6]$, where $[Fe^{III}(CN)_6]^{3-}$ in the electrolyte solution works as the diffusional electron mediator from PSII on the electrode to the electrode substrate. In this diffusional system, a TON of PSII on the electrode was determined to be 3700 ± 800 mol O_2 (mol PSII)$^{-1}$ for 1 h, which was close to the reported value for the colloidal system [6].

4. Conclusions

We have prepared bio–inorganic photoanodes of PSII and ferricyanide-intercalated LDHs and recorded photocurrent responses of them to understand the photo-electrocatalytic activity and stability of PSII. PSII on CoAl–$[Fe(CN)_6]$ LDH/ITO shows the TOF of 0.5±0.1 s^{-1} and the TON of 920 ± 40 for 1 h thanks to ferricyanide intercalated in cationic LDH nanosheets. The photochemical experiments using DCMU and $PSII_{PsbA3}$ suggest that ferricyanide may play an important role in the interfacial electron transfer from Q_A.

Photoelectrochemical measurements using diffusional ferricyanide anions in the

electrolyte solution suggest that there is still some room for improvement in photo-electrocatalytic activity and stability of PSII on CoAl–$[Fe(CN)_6]$ LDH/ITO. For further improvement of photo-electrocatalytic activity and stability of PSII, we need careful interfacial designs not only to achieve efficient interfacial electron transfer but also to make the orientation of PSII suitable for the electron transfer at the electrode interface. Potential candidates would be porous Prussian blue electrodes [49-51], which possibly lead to maximizing the photo-electrocatalytic activity and stability of PSII.

Acknowledgements

The authors thank Dr. Takahiro Nakae for assistance with the SEM experiments. The IR and FE-SEM experiments were carried out at the Integrated Center for Science, Ehime University. This work was supported by JST-PRESTO program (4018 to MS); Grant-in-Aid for Young Scientists (B) (No. 16K20882 to MK); and a MEXT Program for Development of Environmental Technology using Nanotechnology from the Ministry of Education, Culture, Sports, Science and Technology, Japan.

Appendix A. Supplementary data

Supplementary data associated with this article can be found, in the online version, at xxx.

References

[1] M. Suga, F. Akita, K. Hirata, G. Ueno, H. Murakami, Y. Nakajima, T. Shimizu, K. Yamashita, M. Yamamoto, H. Ago, J.-R. Shen, Native structure of photosystem II at 1.95 Å resolution viewed by femtosecond X-ray pulses, Nature, 517 (2014) 99-103.

[2] Y. Umena, K. Kawakami, J.R. Shen, N. Kamiya, Crystal structure of oxygen-evolving photosystem II at a resolution of 1.9 angstrom, Nature, 473 (2011) 55-60.

[3] N. Cox, M. Retegan, F. Neese, D.A. Pantazis, A. Boussac, W. Lubitz, Electronic structure of the oxygenevolving complex in photosystem II prior to O-O bond formation, Science, 345 (2014) 804-808.

[4] T. Kothe, N. Plumere, A. Badura, M.M. Nowaczyk, D.A. Guschin, M. Rogner, W. Schuhmann, Combination of A Photosystem 1-Based Photocathode and a Photosystem 2-Based Photoanode to a Z-Scheme Mimic for Biophotovoltaic Applications, Angew. Chem. Int. Ed., 52 (2013) 14233-14236.

[5] D. Mersch, C.Y. Lee, J.Z. Zhang, K. Brinkert, J.C. Fontecilla-Camps, A.W. Rutherford, E. Reisner, Wiring of Photosystem II to Hydrogenase for Photoelectrochemical Water Splitting, J. Am. Chem. Soc., 137 (2015) 8541-8549.

[6] W.Y. Wang, J. Chen, C. Li, W.M. Tian, Achieving solar overall water splitting with hybrid photosystems of photosystem II and artificial photocatalysts, Nat. Commun., 5 (2014) 5647.

[7] C.X. Zhang, C.H. Chen, H.X. Dong, J.R. Shen, H. Dau, J.Q. Zhao, A synthetic Mn4Ca-cluster mimicking the oxygen-evolving center of photosynthesis, Science, 348 (2015) 690-693.

[8] E.Y. Tsui, T. Agapie, Reduction potentials of heterometallic manganese-oxido cubane complexes modulated by redox-inactive metals, Proc. Natl. Acad. Sci. U.S.A., 110 (2013) 10084-10088.

[9] E.Y. Tsui, R. Tran, J. Yano, T. Agapie, Redox-inactive metals modulate the reduction potential in heterometallic manganese-oxido clusters, Nat Chem, 5 (2013) 293-299.

[10] R.K. Hocking, R. Brimblecombe, L.Y. Chang, A. Singh, M.H. Cheah, C. Glover, W.H. Casey, L. Spiccia, Water-oxidation catalysis by manganese in a geochemical-like cycle, Nat Chem, 3 (2011) 461-466.

[11] S.Y. Reece, J.A. Hamel, K. Sung, T.D. Jarvi, A.J. Esswein, J.J.H. Pijpers, D.G. Nocera, Wireless Solar Water Splitting Using Silicon-Based Semiconductors and Earth-Abundant Catalysts, Science, 334 (2011) 645-648.

[12] M.M. Najafpour, G. Renger, M. Holynska, A.N. Moghaddam, E.M. Aro, R. Carpentier, H. Nishihara, J.J. Eaton-Rye, J.R. Shen, S.I. Allakhverdiev, Manganese Compounds as Water-Oxidizing Catalysts: From the Natural Water-Oxidizing Complex to Nanosized

Manganese Oxide Structures, Chem. Rev., 116 (2016) 2886-2936.
[13] M. Kato, J.Z. Zhang, N. Paul, E. Reisner, Protein film photoelectrochemistry of the water oxidation enzyme photosystem II, Chem. Soc. Rev., 43 (2014) 6485-6497.
[14] W. Lubitz, E.J. Reijerse, J. Messinger, Solar water-splitting into H2 and O2: design principles of photosystem II and hydrogenases, Energ. Environ. Sci., 1 (2008) 15-31.
[15] T. Tyystjarvi, E.M. Aro, C. Jansson, P. Maenpaa, Changes of Amino-Acid-Sequence in Pest-Like Area and Qeeet Motif Affect Degradation Rate of D1 Polypeptide in Photosystem-Ii, Plant. Mol. Biol., 25 (1994) 517-526.
[16] M. Sugiura, A. Boussac, T. Noguchi, F. Rappaport, Influence of Histidine-198 of the D1 subunit on the properties of the primary electron donor, P-680, of photosystem II in Thermosynechococcus elongatus, Biochim. Biophys. Acta, 1777 (2008) 331-342.
[17] M. Sugiura, Y. Inoue, Highly purified thermo-stable oxygen-evolving photosystem II core complex from the thermophilic cyanobacterium Synechococcus elongatus having his-tagged CP43, Plant. Cell. Physiol., 40 (1999) 1219-1231.
[18] S. Khan, J.S. Sun, G.W. Brudvig, Cation Effects on the Electron-Acceptor Side of Photosystem II, J. Phys. Chem. B, 119 (2015) 7722-7728.
[19] G. Ulas, G.W. Brudvig, Redirecting Electron Transfer in Photosystem II from Water to Redox-Active Metal Complexes, J. Am. Chem. Soc., 133 (2011) 13260-13263.
[20] S. Larom, D. Kallmann, G. Saper, R. Pinhassi, A. Rothschild, H. Dotan, G. Ankonina, G. Schuster, N. Adir, The Photosystem II D1-K238E mutation enhances electrical current production using cyanobacterial thylakoid membranes in a bio-photoelectrochemical cell, Photosynth. Res., 126 (2015) 161-169.
[21] S. Larom, F. Salama, G. Schuster, N. Adir, Engineering of an alternative electron transfer path in photosystem II, Proc. Natl. Acad. Sci. U.S.A., 107 (2010) 9650-9655.
[22] M. Kato, T. Cardona, A.W. Rutherford, E. Reisner, Photoelectrochemical Water Oxidation with Photosystem II Integrated in a Mesoporous; Indium Tin Oxide Electrode, J. Am. Chem. Soc., 134 (2012) 8332-8335.
[23] M. Kato, T. Cardona, A.W. Rutherford, E. Reisner, Covalent Immobilization of Oriented Photosystem II on a Nanostructured Electrode for Solar Water Oxidation, J. Am. Chem. Soc., 135 (2013) 10610-10613.
[24] K.P. Sokol, D. Mersch, V. Hartmann, J.Z. Zhang, M.M. Nowaczyk, M. Rogner, A. Ruff, W. Schuhmann, N. Plumere, E. Reisner, Rational wiring of photosystem II to hierarchical indium tin oxide electrodes using redox polymers, Energ. Environ. Sci., 9 (2016) 3698-3709.
[25] J. Li, X. Feng, J. Fei, P. Cai, J. Huang, J. Li, Integrating photosystem II into a porous TiO2 nanotube network toward highly efficient photo-bioelectrochemical cells, J. Mater. Chem. A, 4 (2016) 12197-12204.

[26] K.K. Rao, D.O. Hall, N. Vlachopoulos, M. Gratzel, M.C.W. Evans, M. Seibert, Photoelectrochemical Responses of Photosystem-Ii Particles Immobilized on Dye-Derivatized Tio2 Films, J. Photochem. Photobiol. B, 5 (1990) 379-389.
[27] W. Wang, Z. Wang, Q. Zhu, G. Han, C. Ding, J. Chen, J.-R. Shen, C. Li, Direct electron transfer from photosystem II to hematite in a hybrid photoelectrochemical cell, Chem. Commun., 51 (2015) 16952-16955.
[28] O. Yehezkeli, R. Tel-Vered, D. Michaeli, R. Nechushtai, I. Willner, Photosystem I (PSI)/Photosystem II (PSII)-Based Photo-Bioelectrochemical Cells Revealing Directional Generation of Photocurrents, Small, 9 (2013) 2970-2978.
[29] O. Yehezkeli, R. Tel-Vered, J. Wasserman, A. Trifonov, D. Michaeli, R. Nechushtai, I. Willner, Integrated photosystem II-based photo-bioelectrochemical cells, Nat. Commun., 3 (2012) 742.
[30] A. Badura, D. Guschin, B. Esper, T. Kothe, S. Neugebauer, W. Schuhmann, M. Rogner, Photo-induced electron transfer between photosystem 2 via cross-linked redox hydrogels, Electroanal, 20 (2008) 1043-1047.
[31] N. Keren, A. Berg, P.J.M. VanKan, H. Levanon, I. Ohad, Mechanism of photosystem II photoinactivation and D1 protein degradation at low light: The role of back electron flow, Proc. Natl. Acad. Sci. U.S.A., 94 (1997) 1579-1584.
[32] J.B. Han, Y.B. Dou, J.W. Zhao, M. Wei, D.G. Evans, X. Duan, Flexible CoAl LDH@PEDOT Core/Shell Nanoplatelet Array for High-Performance Energy Storage, Small, 9 (2013) 98-106.
[33] J.W. Zhao, M.F. Shao, D.P. Yan, S.T. Zhang, Z.Z. Lu, Z.X. Li, X.Z. Cao, B.Y. Wang, M. Wei, D.G. Evans, X. Duan, A hierarchical heterostructure based on Pd nanoparticles/layered double hydroxide nanowalls for enhanced ethanol electrooxidation, J. Mater. Chem. A, 1 (2013) 5840-5846.
[34] M. Gong, Y.G. Li, H.L. Wang, Y.Y. Liang, J.Z. Wu, J.G. Zhou, J. Wang, T. Regier, F. Wei, H.J. Dai, An Advanced Ni-Fe Layered Double Hydroxide Electrocatalyst for Water Oxidation, J. Am. Chem. Soc., 135 (2013) 8452-8455.
[35] X. Zou, A. Goswami, T. Asefa, Efficient Noble Metal-Free (Electro)Catalysis of Water and Alcohol Oxidations by Zinc-Cobalt Layered Double Hydroxide, J. Am. Chem. Soc., 135 (2013) 17242-17245.
[36] Z. Lu, W.W. Xu, W. Zhu, Q. Yang, X.D. Lei, J.F. Liu, Y.P. Li, X.M. Sun, X. Duan, Three-dimensional NiFe layered double hydroxide film for high-efficiency oxygen evolution reaction, Chem. Commun., 50 (2014) 6479-6482.
[37] S. Un, A. Boussac, M. Sugiura, Characterization of the tyrosine-Z radical and its environment in the spin-coupled S(2)Tyr(Z)(center dot) state of photosystem II from

Thermosynechococcus elongatus, Biochemistry, 46 (2007) 3138-3150.
[38] S. Ogami, A. Boussac, M. Sugiura, Deactivation processes in PsbA1-Photosystem II and PsbA3-Photosystem II under photoinhibitory conditions in the cyanobacterium Thermosynechococcus elongatus, Biochim. Biophys. Acta, 1817 (2012) 1322-1330.
[39] X. Guo, F.Z. Zhang, S.L. Xu, D.G. Evans, X. Duan, Preparation of layered double hydroxide films with different orientations on the opposite sides of a glass substrate by in situ hydrothermal crystallization, Chem. Commun., 45 (2009) 6836-6838.
[40] N. Iyi, T. Matsumoto, Y. Kaneko, K. Kitamura, Deintercalation of carbonate ions from a hydrotalcite-like compound: Enhanced decarbonation using acid-salt mixed solution, Chem. Mater., 16 (2004) 2926-2932.
[41] Z.P. Liu, R.Z. Ma, M. Osada, N. Iyi, Y. Ebina, K. Takada, T. Sasaki, Synthesis, anion exchange, and delamination of Co-Al layered double hydroxide: Assembly of the exfoliated nanosheet/polyanion composite films and magneto-optical studies, J. Am. Chem. Soc., 128 (2006) 4872-4880.
[42] A. Commet, N. Boswell, C.F. Yocum, H. Popelka, pH Optimum of the Photosystem II H2O Oxidation Reaction: Effects of PsbO, the Manganese-Stabilizing Protein, Cl– Retention, and Deprotonation of a Component Required for O2 Evolution Activity, Biochemistry, 51 (2012) 3808-3818.
[43] R.J. Porra, The chequered history of the development and use of simultaneous equations for the accurate determination of chlorophylls a and b, Photosynth. Res., 73 (2002) 149-156.
[44] J.B. Qiu, G. Villemure, Anionic clay modified electrodes: Electron transfer mediated by electroactive nickel, cobalt or manganese sites in layered double hydroxide films, J. Electroanal. Chem., 428 (1997) 165-172.
[45] G. Layrac, D. Tichit, J. Larionova, Y. Guari, C. Guerin, Controlled Growth of Cyano-Bridged Coordination Polymers into Layered Double Hydroxides, J. Phys. Chem. C, 115 (2011) 3263-3271.
[46] W. Tischer, H. Strotmann, Relationship between Inhibitor Binding by Chloroplasts and Inhibition of Photosynthetic Electron-Transport, Biochim. Biophys. Acta, 460 (1977) 113-125.
[47] M. Sugiura, A. Boussac, Some Photosystem II properties depending on the D1 protein variants in Thermosynechococcus elongatus, Biochim. Biophys. Acta, 1837 (2014) 1427-1434.
[48] Y. Kato, T. Shibamoto, S. Yamamoto, T. Watanabe, N. Ishida, M. Sugiura, F. Rappaport, A. Boussac, Influence of the PsbA1/PsbA3, Ca2+/Sr2+ and Cl-/Br- exchanges on the redox potential of the primary quinone Q(A) in Photosystem II from Thermosynechococcus elongatus as revealed by spectroelectrochemistry, Biochim. Biophys. Acta, 1817 (2012) 1998-2004.
[49] B. Kong, C. Selomulya, G.F. Zheng, D.Y. Zhao, New faces of porous Prussian blue: interfacial assembly of integrated hetero-structures for sensing applications, Chem. Soc. Rev.,

44 (2015) 7997-8018.
[50] S.C. Jang, Y. Haldorai, G.W. Lee, S.K. Hwang, Y.K. Han, C. Roh, Y.S. Huh, Porous three-dimensional graphene foam/Prussian blue composite for efficient removal of radioactive Cs-137, Sci Rep-Uk, 5 (2015).
[51] B.A. Kong, X.T. Sun, C. Selomulya, J. Tang, G.F. Zheng, Y.Q. Wang, D.Y. Zhao, Sub-5 nm porous nanocrystals: interfacial site-directed growth on graphene for efficient biocatalysis, Chem Sci, 6 (2015) 4029-4034.

Figure captions

Fig. 1. Schematic representation of the oxygen evolution driven by MAl–$[Fe(CN)_6]$|PSII (M = Mg or Co) photoanodes under visible light irradiation.

Fig. 2. Top-view and cross-sectional SEM images of (a,b) the as-prepared MgAl–CO_3 LDH and (c,d) CoAl–CO_3 LDH on ITO-coated glass substrates. The film thicknesses of MgAl–CO_3 and CoAl–CO_3 LDHs are approximately 0.6 μm and 3.3 μm, respectively.

Fig. 3. (A) Representative photocurrent responses of (a) MgAl–CO_3 (no PSII), (b) MgAl–CO_3|PSII, (c) MgAl–$[Fe(CN)_6]$ (no PSII), (d) MgAl–$[Fe(CN)_6]$|PSII, (e) CoAl–CO_3 (no PSII), (f) CoAl–CO_3|PSII, (g) CoAl–$[Fe(CN)_6]$ (no PSII), (h) CoAl–$[Fe(CN)_6]$|Mn–depleted PSII and (i) CoAl–$[Fe(CN)_6]$|PSII. The photocurrent responses were recorded in a buffered solution containing 40 mM 2-(*N*-morpholino)ethanesulfonic acid (MES), 15 mM $CaCl_2$, 15 mM $MgCl_2$ and 100 mM NaCl at pH 6.5. The arrows indicate the start (ON) and end (OFF) of light irradiation (> 600 nm, 10 mW cm^{-2}). (B) Representative photocurrent decay of CoAl–$[Fe(CN)_6]$|PSII over 1 h under the red light irradiation.

Fig. 4. Photocurrent action spectrum of CoAl–$[Fe(CN)_6]$|PSII recorded at +0.5 V vs NHE, where IPCEs were plotted against wave lengths of the incident light. An absorption spectrum of PSII in the electrolyte solution was also shown in the gray trace.

Figures

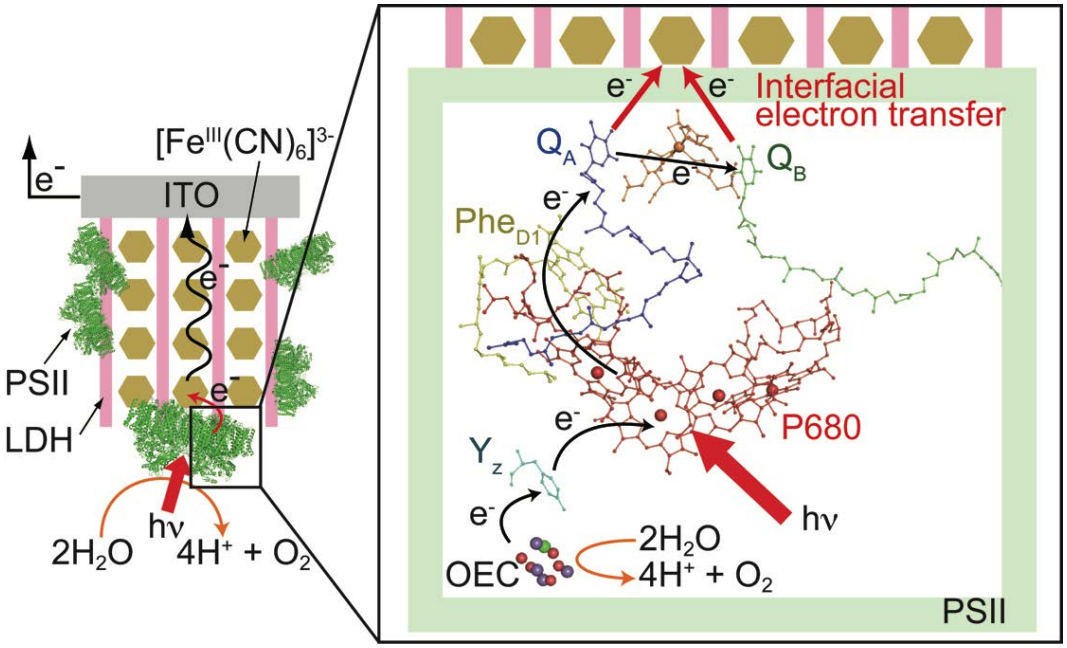

Fig. 1

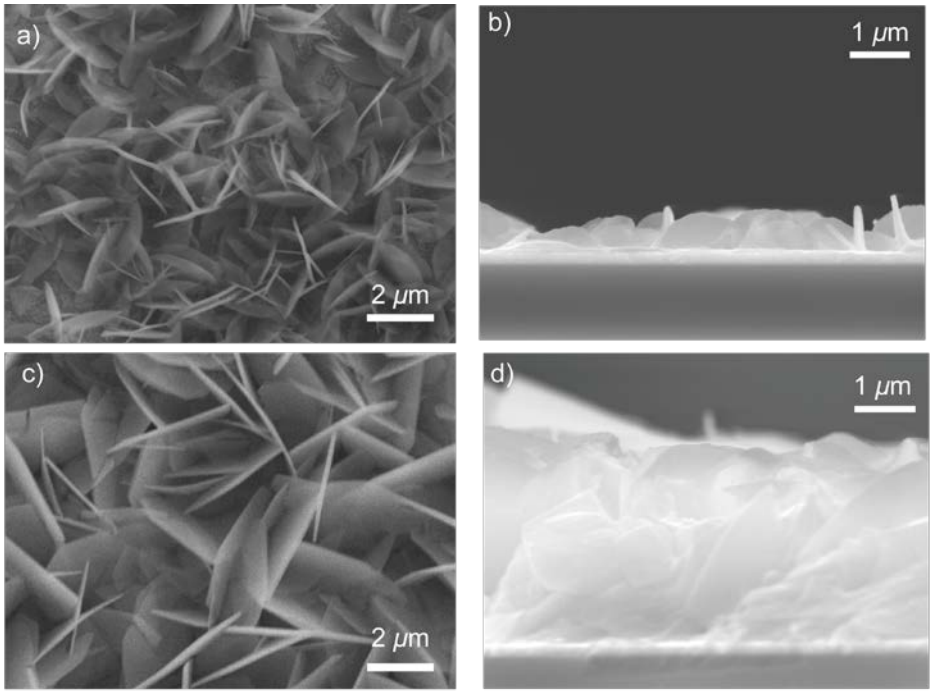

Fig. 2

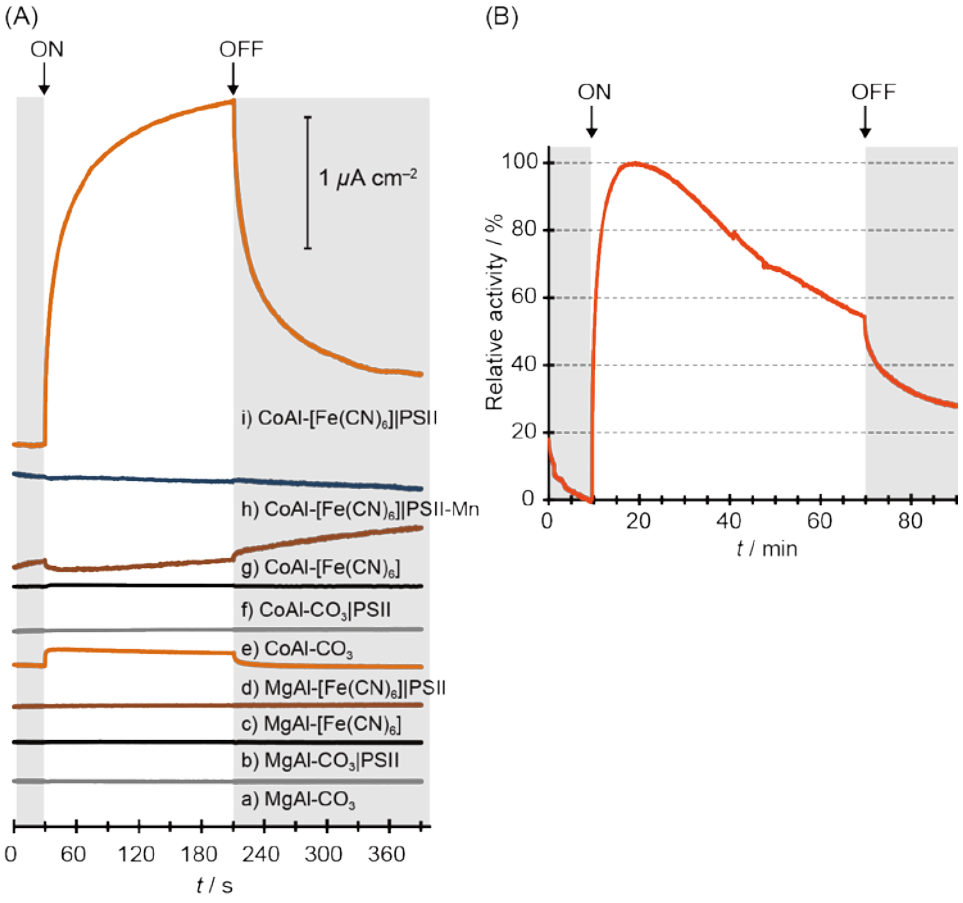
(A)
ON
OFF
1 μA cm⁻²
i) CoAl-[Fe(CN)6]|PSII
h) CoAl-[Fe(CN)6]|PSII-Mn
g) CoAl-[Fe(CN)6]
f) CoAl-CO3|PSII
e) CoAl-CO3
d) MgAl-[Fe(CN)6]|PSII
c) MgAl-[Fe(CN)6]
b) MgAl-CO3|PSII
a) MgAl-CO3
0 60 120 180 240 300 360
t / s
(B)
ON
OFF
Relative activity / %
0 20 40 60 80 100
0 20 40 60 80
t / min

Fig. 3

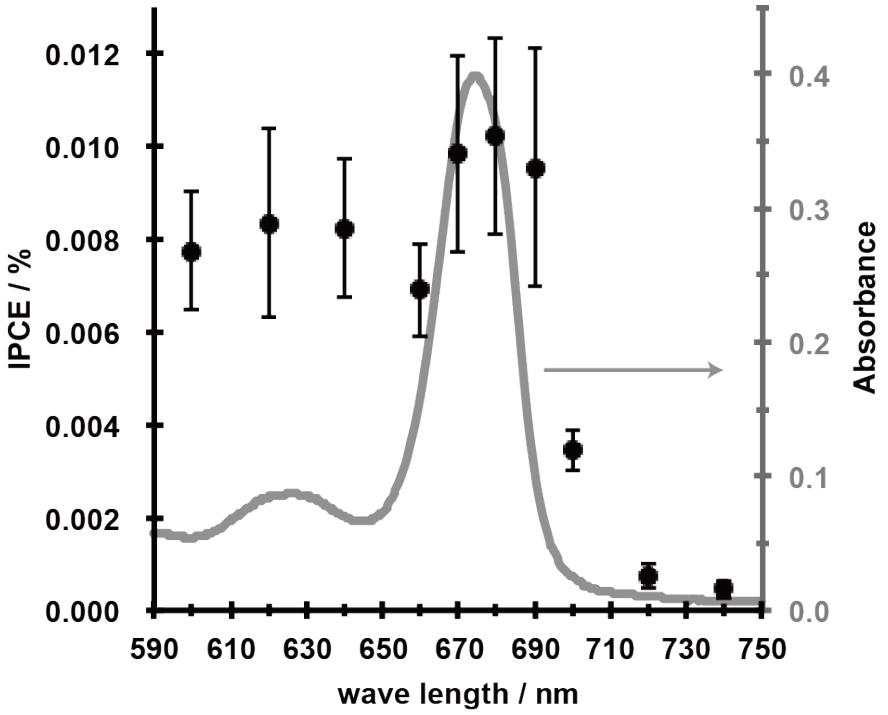
0.012
0.010
0.008
0.006
0.004
0.002
0.000
IPCE / %
0.4
0.3
0.2
0.1
0.0
Absorbance
590
610
630
650
670
690
710
730
750
wave length / nm

Fig. 4

Table caption

Table 1. Summary of photocurrent densities, amounts of PSII immobilized on electrodes and TOFs of MAl–$[Fe(CN)_6]$|PSII.

Table 1.

Electrode	j / μA cm^{-2} [a]	PSII / pmol[b]	TOF / s^{-1}[c]
MgAl–[FeCN)$_6$]|PSII	0.07±0.02	1.7±0.6	0.07±0.03
CoAl–[FeCN)$_6$]|PSII	2.3±0.2	7.1±0.5	0.5±0.1
CoAl–[FeCN)$_6$]|PSII with DCMU [d]	1.3±0.2	7.8±0.2	0.22±0.03
CoAl–[FeCN)$_6$]|PSII$_{PsbA3}$ [e]	1.0±0.3	7.1±0.6	0.18±0.04

[a] Normalized to the projected geometric surface area of the electrode (0.5 cm^2) and recorded at +0.5 V vs NHE in the electrolyte solution containing 40 mM MES, 15 mM $CaCl_2$, 15 mM $MgCl_2$ and 100 mM NaCl at pH 6.5 under red light irradiation (> 600 nm, 10 mW cm^{-2}). [b] Amounts of PSII per electrode were determined from UV-vis absorption spectra of Chlorophyll *a* extracted from PSII immobilized on electrodes. [c] TOFs in mol O_2 (mol PSII)$^{-1}$ were calculated from the amounts of PSII and photocurrent densities assuming 100% of electrons collected by the electrode were consumed for the O_2 evolution by PSII. [d] The electrolyte solution containing 1 mM DCMU was used. [e] PSII$_{PsbA3}$ was used.